Intermetallic Phase Formation in Al-Si-Zr Alloys During Hot Isostatic Pressing Revealed by Experiments and Molecular Dynamics

Ankit Roy[1, Γ], Rajib Kalsar[1], James V. Haag IV[1] and Vineet V. Joshi[1, Γ]
[1] *Pacific Northwest National Laboratory, Richland, WA 99354, USA*

Abstract

Understanding phase transformations at alloy interfaces is critical for the design of advanced structural materials. In this study, we investigate the formation mechanisms of the Al_2SiZr intermetallic phase in the Al-Si-Zr system under hot isostatic pressing (HIP) using molecular dynamics (MD) simulations and thermodynamic analysis. A unique aspect of our approach in MD involves the replacement of a disordered Al_2SiZr stoichiometry with an ordered phase at the Al-Zr interface once HIP results in the desired Al_2SiZr stoichiometry, allowing us to compute the total energetic cost of transformation by accounting for both formation energies and diffusion barriers. Diffusion coefficients and activation energies, extracted across a range of temperatures, reveal that HIP substantially enhances atomic mobility, creating favorable stoichiometry for phase evolution. Our results show that Al_2SiZr phase formation is kinetically unfavorable at lower temperatures but becomes feasible when the thermodynamic driving energy surpass a critical energy threshold.

[Γ] Corresponding authors. Email: ankit.roy@pnnl.gov, vineet.joshi@pnnl.gov.

Introduction

The Al-Zr binary system [1-4] has garnered significant attention within the materials science community, primarily due to beneficial phase transformations during manufacturing processes such as hot isostatic pressing (HIP) [5, 6]. HIP enhances the mechanical properties and structural integrity of materials through application of high temperature and pressure. HIP also catalyzes complex interdiffusion phenomena within the Al-Zr matrix leading to the formation of intermetallic phases [1, 2]. The inclusion of silicon atoms at the Al-Zr interface can alter the thermodynamics and kinetics of phase development [1]. Its presence modifies the energetics at the atomic level facilitating the nucleation and growth of some desirable intermetallic phases. Through molecular dynamics (MD) simulations, one can explore the depth of these transformations by calculating the thermodynamic driving forces or the reduction in system energy associated with secondary phase development [7].

The inception of the Reduced Enrichment for Research and Test Reactors (RERTR) program in 1978 marked a transition from high-enriched uranium fuel to low-enriched uranium solutions, driven by global nuclear non-proliferation commitments [1]. While the development of uranium-silicide dispersion fuels with densities ranging between 2.3 and 4.8 g-U/cm^3 successfully facilitated the conversion of nearly 90% of reactors, the target for even higher uranium densities necessitated innovative fuel designs [8]. Monolithic fuel plates, notably those incorporating U-10 wt.% Mo (U-10Mo) fuels with an AA6061 cladding, represent a frontier in achieving the requisite fuel densities [9, 10]. However, the adverse effects of fuel-cladding chemical interactions (FCCI) under irradiation conditions remains a critical challenge, as they lead to the emergence of porous layers that compromise mechanical integrity and thermal conductivity [9-12]. The use of zirconium as a diffusion barrier is a remedy, with zirconium mitigating FCCI and ensuring structural integrity [4]. Experimental validations have shown that the introduction of a Zr barrier preserves the integrity of both fuel-barrier and barrier-cladding interfaces post-irradiation, avoiding bubble formation and maintaining mechanical stability [13, 14]. Thus, a systematic characterization and theoretical understanding of the interdiffusion between the barrier and cladding materials becomes imperative. This study aspires to unravel these interactions through an integration of MD simulations and experimental insights, adding to the foundational knowledge necessary for the development of next-generation nuclear fuel technologies.

This study aims to identify the diffusional interactions between a Zr diffusion barrier and AA6061 cladding and quantify the thermodynamics of observed phase transformation. Utilizing MD simulations complemented by experimental observations, we analyze the Al-Zr interface incorporating Si atoms, investigating secondary phase formation during hot isostatic pressing of Al-Zr with Si at the interface. Our fundamental calculations within the MD simulations reveal that the energy drop associated with secondary phase formation primarily drives intermetallic formation. Diffusion coefficients for Al, Zr, and Si were obtained to complement the thermodynamics of phase transformation.

Methods

Experiments

To support the conversion the United States Advanced Research and Test Reactor from high-enriched uranium (HEU) to low-enriched uranium (LEU), metallic monolithic fuel is being fabricated using hot isostatic pressing (HIP) of U-10Mo foil encapsulated by Al 6061-T6 plates. The specific processing parameters and procedures are detailed in the referenced literatures [5, 6, 15, 16]. HIP was conducted at temperatures 450 and 560°C for a duration of 1.5 hours under an applied pressure of 103 MPa. To investigate diffusion mechanisms and facilitate process optimization, Zr foil was sandwiched between two Al6061 plates and subjected to bonding at the same HIP conditions (450 and 560°C). The thickness of Al6061 plate (composition in wt.%, Mg: 0.90, Si: 0.73, Cu: 0.31, Fe: 0.47, Cr: 0.20, Mn: 0.08, Zn: 0.11, Ti: 0.03, Al: bal) and Zr (99.9% purity) foil was approximately 1.2 mm and 0.203 mm, respectively.

Scanning electron microscopy (SEM) was utilized to characterize the interfacial microstructure and elemental distribution at the Al/Zr interface. Microstructural and compositional analyses were performed using a JEOL JSM-7600F field emission SEM equipped with an Oxford Instruments Aztec X-Max 80 mm^2 energy-dispersive X-ray spectroscopy (EDS) system. Typical SEM operating parameters included an accelerating voltage of 15 keV, a working distance of 15 mm, a 110 μm aperture, and an electron beam current of 6 nA or higher. Elemental profiling across the Al/Zr interface was conducted using EDS line scan analysis.

Thin film lamellae specimens were prepared targeting the HIP bonded interfaces from the 450ºC and 560ºC conditions for transmission electron microscopy (TEM) and scanning transmission electron microscopy (STEM) analyses. Specimen foils were lifted out of the material bulk and thinned to electron transparency via focused ion beam (FIB) milling with Ga+ ions on an FEI Quanta scanning electron microscope (SEM). The resulting FIB lamellae were characterized using a probe corrected JEOL ARM operated at 200kV. To probe the chemical environment of the interfacial regions, the samples were subjected to STEM-EDS analysis. Characteristic x-ray spectra were acquired on a JEOL Centurio EDS detector, with all data processed using Thermo Fisher's Pathfinder software. For crystal structure determination, multiple selected area diffraction patterns (SADP) were acquired, and have been compared with the simulated diffraction result using SingleCrystal version 5.2.1.

Computer simulation methods

To model the Al-Zr-Si system in LAMMPS [17], an interatomic potential is essential to accurately describe the interactions between the constituent elements. Unfortunately, a direct interatomic potential that encompasses all three elements is not readily available in existing literature. To overcome this challenge, we adopted a combinatorial approach, integrating individual Tersoff potentials for Al, Zr and Si. Specifically, the Tersoff parameters for Al were sourced from Plummer et al. [18], those for Zr from Daw et al. [19], and for Si from the work by Tersoff in 1988 [20]. This combinatorial model was implemented using a Python code developed by Kristensen et al. [21], which facilitates the merging of distinct Tersoff potential parameters into a coherent framework suitable for modeling multi-component systems. The resultant Al-Si-Zr potential generated through the combinatorial approach is detailed in Supplementary Table S1. To validate the potential's efficacy in modeling alloy systems, we examined the bond lengths within the Al_2SiZr phase with those in Materials project database [22] that has been explored in the current study.

Diffusion bonding simulations were conducted utilizing methodologies consistent with our prior work as detailed in Roy et al. [7]. The simulation domain comprised a 25 nm × 12.5 nm × 12.5 nm setup featuring approximately 110,000 atoms, representing an interface between aluminum (Al) and zirconium (Zr), with an intervening monolayer of silicon (Si). In the constructed Al–Zr interface model, the FCC-Al and HCP-Zr slabs have the [100] axis aligned along the interface normal (x-direction), and their (100) planes forming the interface. The orientation relationship is therefore Al(100) || Zr($1\bar{1}00$. To accurately mimic realistic conditions, periodic boundary conditions were employed in all spatial directions, ensuring continuity across the simulated sample. The system was initially equilibrated in the microcanonical ensemble (NVE) for 50 ps, preparing it for the subsequent hot isostatic pressing (HIP) simulations.

The MD simulation representing HIP involved compressing the system with a controlled engineering strain rate, reducing the box dimensions linearly to 92% of their initial values over a duration of 1 ns. To maintain thermal consistency, a Berendsen thermostat was deployed, rescaling atomic velocities at each timestep to sustain the target temperatures. The simulations were done across a broad temperature range of 300 K, 673 K, 723 K, 773 K, and 823 K and diffusion was measured using mean square displacements (MSD) [23, 24]. Postprocessing of the simulation data enabled the analysis of interfacial stoichiometry and thickness evolution over time and temperature. At around 1 ns, the interfacial zone consisting of Al, Si, and Zr attained a stoichiometry approximating Al_2SiZr.

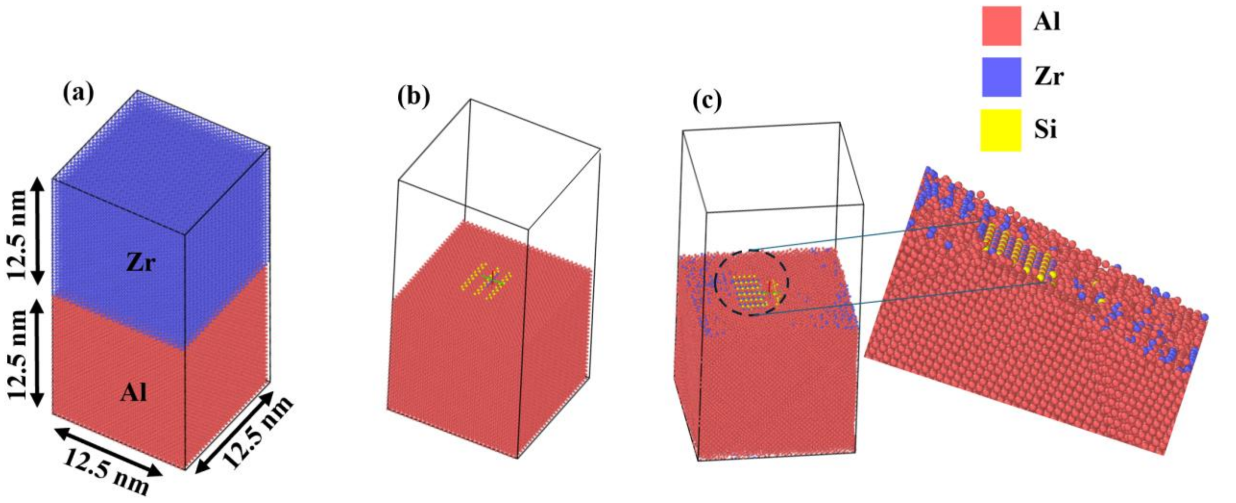

Figure 1: (a) The initial configuration illustrating the interface between the Al and Zr regions prior to processing. (b) A detailed cross-sectional view of the Al-Zr interface, highlighting the incorporation of 380 silicon (Si) atoms embedded within the interfacial layer. (c) The transformed interfacial region, demonstrating the replacement of the Al_2SiZr stoichiometry with a systematically ordered intermetallic structure subsequent to the completion of the hot isostatic pressing (HIP) process.

Upon achieving this composition, the HIP process was halted, and the resultant atomic configuration was extracted for further analysis. Two distinct simulations were subsequently initiated. The first simulation, conducted in an isothermal-isobaric ensemble (NVT), evaluated the internal energy of the HIP-processed system within its compressed state. The second simulation involved a slightly altered setup, where the Al_2SiZr-stoichiometric region was excised and substituted with the known intermetallic structure of Al_2SiZr, as depicted in Figure 1. In the constructed Al–Zr–Al_2SiZr interface model, the intermetallic Al_2SiZr phase is inserted between FCC-Al and HCP-Zr slabs, with its [100] axis aligned along the interface normal (x-direction), and its (100) plane forming the interface with both Al and Zr. The orientation relationship is therefore Al(100) || Al_2SiZr(100) || Zr($1\bar{1}00$). This modified system sought to replicate conditions as if the intermetallic phase had formed in situ during the HIP operation. Another alternative orientation was tested to check the effect of orientation on the energetics of secondary phase formation. This rotated orientation of the Al_2SiZr phase was achieved by a 90° rotation around the y-axis. After rotation, the intermetallic was embedded such that its [–100] axis aligns with the interface normal (x-direction), and its (001) plane interfaces with both the FCC-Al and HCP-Zr slabs. The orientation relationship becomes Al(100) || Al_2SiZr(001) || Zr($1\bar{1}00$).

The modified multiphase system underwent relaxation in the NVT ensemble, maintaining constant volume and temperature to mirror the conditions of the compressed system. Both systems' energies were meticulously recorded over 200 ps. By comparing these energy profiles, the driving thermodynamic force for secondary phase formation was quantified at each studied temperature.

Results and discussion

Figure 2 (a) and b) represent the SEM and EDS maps of samples subjected to HIP at 450 and 560 °C respectively. The SEM images of the samples reveal very thin Al-Zr phases, while intermetallic phases are clearly visible in the sample processed at 560°C. In both the cases, Si-enrichment is observed, with a more pronounced presence in the 560°C HIP sample. To assess the elemental distribution across the boundary, an EDS-line scan was performed along the Al/Zr interface. The elemental distribution in Figure 2 (c) and (d) illustrate the inter-diffusion of Al and Zr, along with Si-enrichment at the interface.

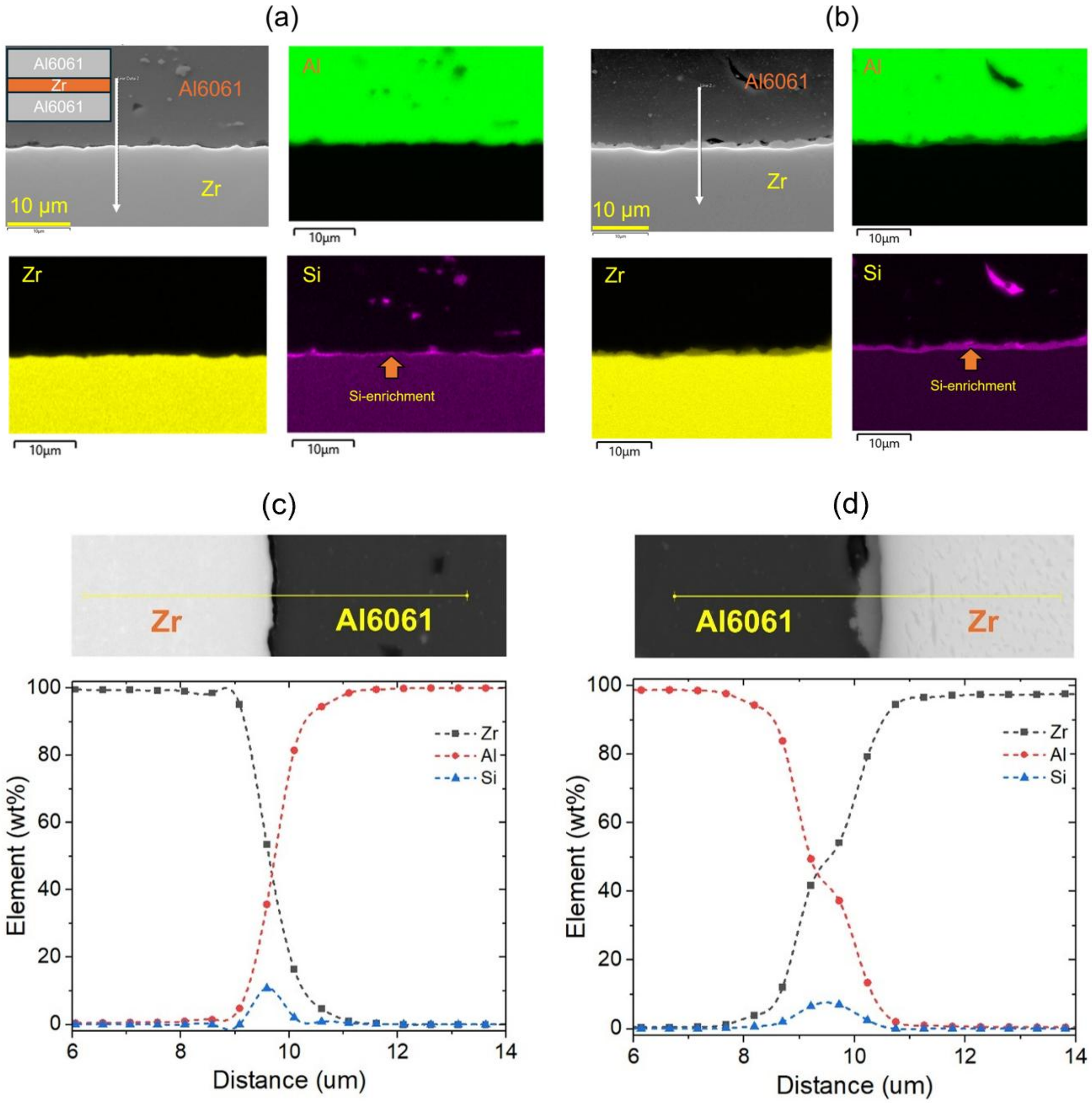

Figure 2. SEM-EDS maps of samples subjected to HIP at 103 MPa for 1.5 hours: (a) processed at 450°C and (b) at 560°C temperature. The inset in (a) illustrates the stacking sequence of the Al6061plate and Zr foil. SEM-EDS line scans of samples HIP'ed at 103 MPa for 1.5 hours: (c) processed at 450°C and (d) at 560°C temperature. The EDS line scan was performed across the interface, as indicated by the white arrow in (a) and (b).

To understand the role of temperature on interfacial structure and bonding the 450 and 560°C processing conditions were characterized via STEM. **Figure 3** exhibits the interface between the Al and Zr in both specimens. The 450°C condition in **Figure 3 (a)** presents evidence of limited intermetallic formation near the Al-Zr interface on the order of 50-100 nm in size. This intermetallic phase is notably discontinuous with apparent regions of interfacial porosity, indicating incomplete interfacial bonding. In contrast, the 560°C condition in **Figure 3 (b)** presents a continuous layer of chemical intermixing and new phase precipitation approximately 500-600nm in thickness. This intermixing layer is notably complex, presenting evidence of multiple phases and chemical interdiffusion across the interface.

STEM-EDS of the specimens helps to further reveal the role of temperature in interfacial bonding. EDS of the 450°C condition in **Figure 3 (a)** presents a thin band of Mg, Si, and O enrichment at the Al-Zr interface. **Figure 3 (b)** from the 560°C condition shows a wider chemical intermixing region consisting primarily of Al-Zr-Si, alongside a thin band of a Mg-rich oxide phase. The formation of the oxide is facilitated by magnesium diffusion at elevated temperatures. Mg diffuses outward and reacts with the native γ-Al_2O_3 layer; which forms immediately on the surface on 6061**;** leading to the formation of a more stable mixed oxide spinel phase ($MgAl_2O_4$)**.** This spinel structure is known to be adherent and thermodynamically stable, especially under prolonged thermal exposure [25]. There is an evident gradient of Si in this Al-Zr-Si, with the Zr-side of the interface presenting the highest concentration.

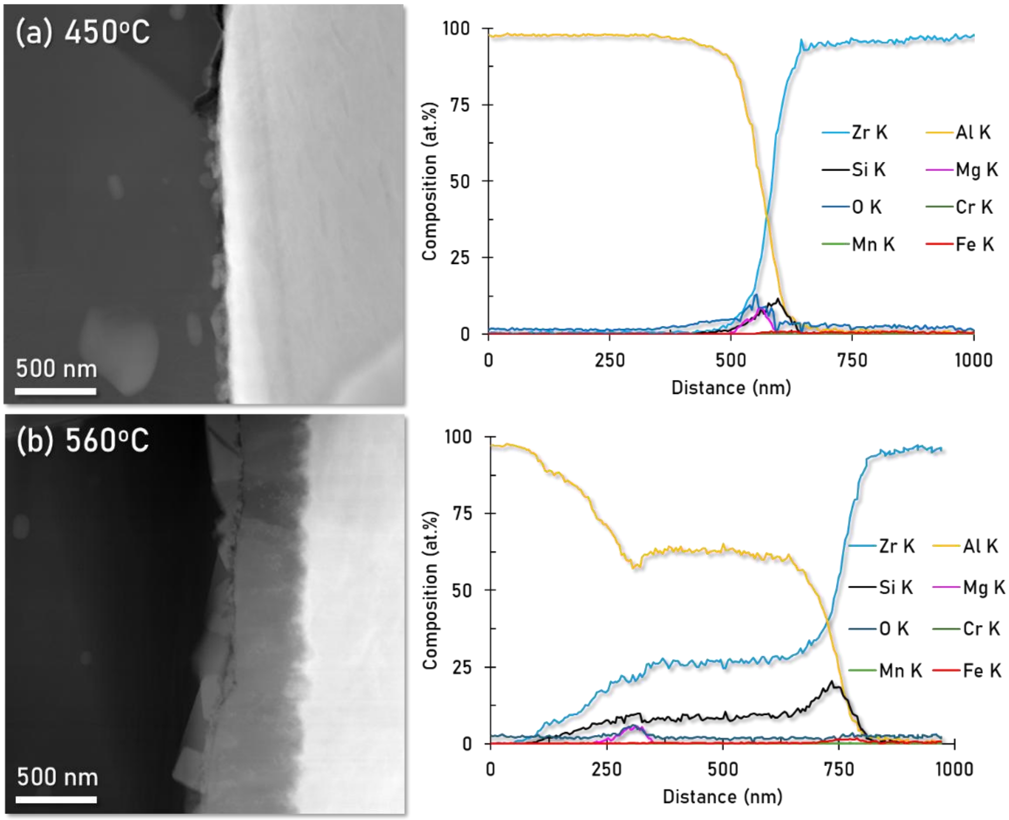

Figure 3. ADF-STEM images of the Al–Zr interface after HIP at (a) 450 °C and (b) 560 °C clearly showing the effect of processing temperature on interfacial structure. At 450 °C, a thin intermetallic layer (~50–100 nm) and interfacial porosity are observed. In contrast, the 560 °C condition shows a continuous (~500–600 nm) layer with evidence of multiphase formation.

To confirm the crystallography of this boundary phase, a single grain from the boundary of the 560°C specimen was oriented to multiple zone axes for TEM diffraction. The grain of interest has been shown in Figure 4a. The acquired diffraction results in Figures 4 (b), (c), and (d) have been compared to the known phases in the Al-Si-Zr system and are noted to match with the tetragonal Al_2SiZr phase. The predicted diffraction patterns for the Al_2SiZr phase have been provided below each experimental diffraction pattern to highlight the degree of matching. The indexed $[\bar{1}00]$ pattern has been provided in the supplementary figure S1, along with a table comparing measured and expected interplanar spacings. The calculated error between the experimentally measured and expected values are noted to be ~5.1% or less, indicating a good structural match.

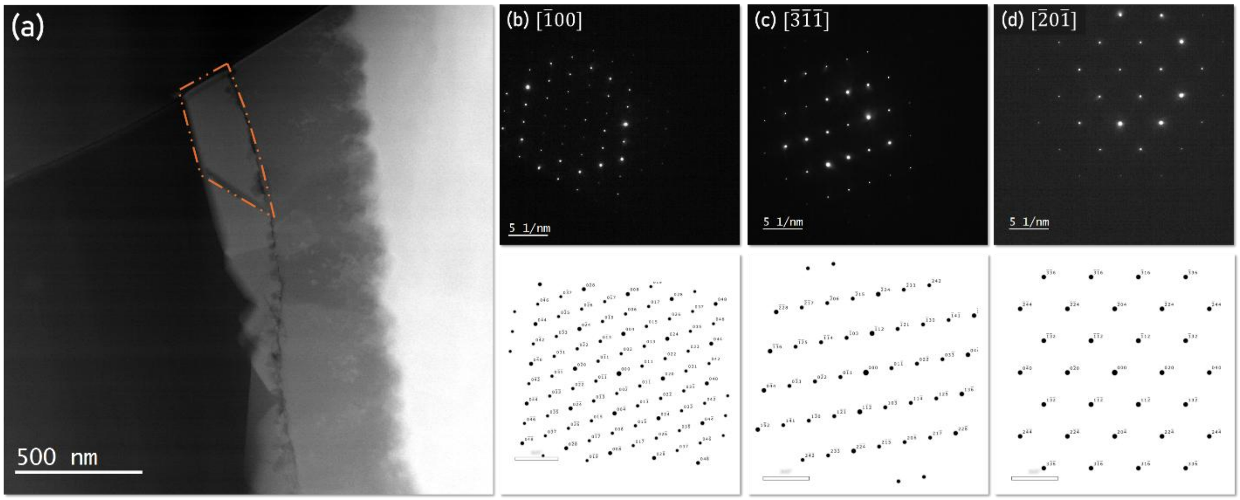

Figure 4: TEM diffraction from multiple zone axes from a single grain of the interfacial precipitate phase. (a) ADF STEM micrograph showing the grain of interest. (b), (c), and (d) diffraction patterns acquired from the $[\bar{1}00]$, $[\bar{3}\bar{1}\bar{1}]$, and $[\bar{2}0\bar{1}]$ respectively alongside the predicted diffraction pattern at that orientation for the tetragonal $ZrAl_2Si$ phase.

In the Al-Si-Zr system, formation of various intermetallic phases such as Al_5SiZr_2, Al_3SiZr_2 , $(Al,Si)_2Zr$ and $(Al,Si)_3Zr$ and can take place [1, 2]. While MD simulations do not inherently involve electron exchange, the evolution of local stoichiometry can be indicative of probable intermetallic phases that might form at interfaces. In our simulations, following 1 ns of HIP deformation, the stoichiometry observed closely aligns with the composition Al_2SiZr. Thus, our study is primarily concentrated on this specific intermetallic phase. Given that MD simulations encompass short durations with accelerated time scales, capturing the formation of all experimentally observed phase stoichiometries within the simulation is impractical. Therefore, we have directed our focus to the Al_2SiZr phase. In validating the MD potentials used in this study, the structure and density properties of Al_2SiZr are compared with DFT values. The individual Tersoff potentials for Al, Zr, and Si have been effectively combined to represent the interactions within the Al_2SiZr phase. The critical interaction zone under HIP conditions is at the interface where these three elements coalesce to form Al_2SiZr, thus validating this interface-specific potential is sufficient. Figure 5 (a) and 5 (b) depict the initial and relaxed states of the Al_2SiZr structure, with Figure 5 (b) illustrating slight atomic displacements from their ideal lattice positions.

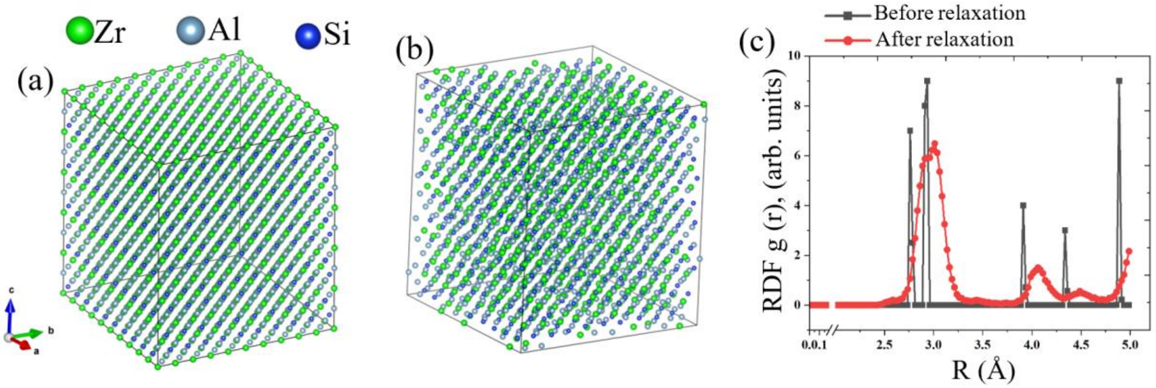

Figure 5: (a) Initial configuration of the Al_2SiZr structure prior to relaxation simulations in MD. (b) Final configuration of the Al_2SiZr after MD relaxation simulations, showing the slight displacements of atoms from their ideal lattice positions. (c) RDF analysis comparing the initial and relaxed states, illustrating changes in atomic spacing and coordination as determined by the applied interatomic potential.

The radial distribution function (RDF) shown in Figure 5 (c) reveals some loss of structural coordination evidenced by the reduced sharpness of peaks, yet the peaks after relaxation (at radial distances 3.01 Å and 4.08 Å) remain reasonably consistent with the initial structure (at 2.93 Å and

3.91 Å). Comparison of MD simulation results with DFT values from the Materials Project highlights discrepancies, such as a 3.95 gm/cc density from MD versus a 4.31 gm/cc density from DFT. This deviation reflects the potential's limitations, as seen in the overestimated volume and slightly increased lattice constants (4.05 versus 3.92 Å and 8.97 versus 8.69 Å), yet with an error margin around 3%, these results are acceptable.

Table 1: Calculated bond distances from MD optimized systems of γ-Al_2O_3 compared with DFT results.

Lattice parameters (Å)	**Tersoff**	**DFT [22]**
a	4.05	3.92
b	4.05	3.92
c	8.97	8.69
Bond distances		
Al-Zr (shorter)	2.74 ± 0.02	2.77
Al-Zr (longer)	3.05 ± 0.03	2.93
Al-Si (shorter)	2.78 ± 0.03	2.77
Al-Si (longer)	2.99 ± 0.03	2.93
Al-Al	3.05 ± 0.03	2.93
Density (gm/cc)	3.95	4.31

The deviation in density of 3.95 gm/cc obtained from MD vs 4.31 gm/cc from DFT is acknowledged as a shortcoming of the compiled potential. The volume is slightly overestimated from this potential which is also reflected in the increased lattice constants 4.05 vs 3.92 Å and 8.97 vs 8.69 Å. Since this is just a little over 3% it can be considered acceptable.

The HIP simulation results offer insights into atomic migration across the Al-Zr interface, at elevated temperature and pressure conditions. Typically, temperatures in the range of 0.6-0.8 times the melting temperature (T_m) are necessary to facilitate this migration. Considering Al melting point is approximately 933 K, the temperatures studied here (300 K – 823 K) are adequate for simulating interfacial diffusion. As shown in Figure 6 (a), simulations conducted at 823 K reveal an increased migration of Al atoms into the Zr region, higher than the reverse migration of Zr atoms into the Al zone, as depicted qualitatively in Figures 6 (b) and 6 (c).

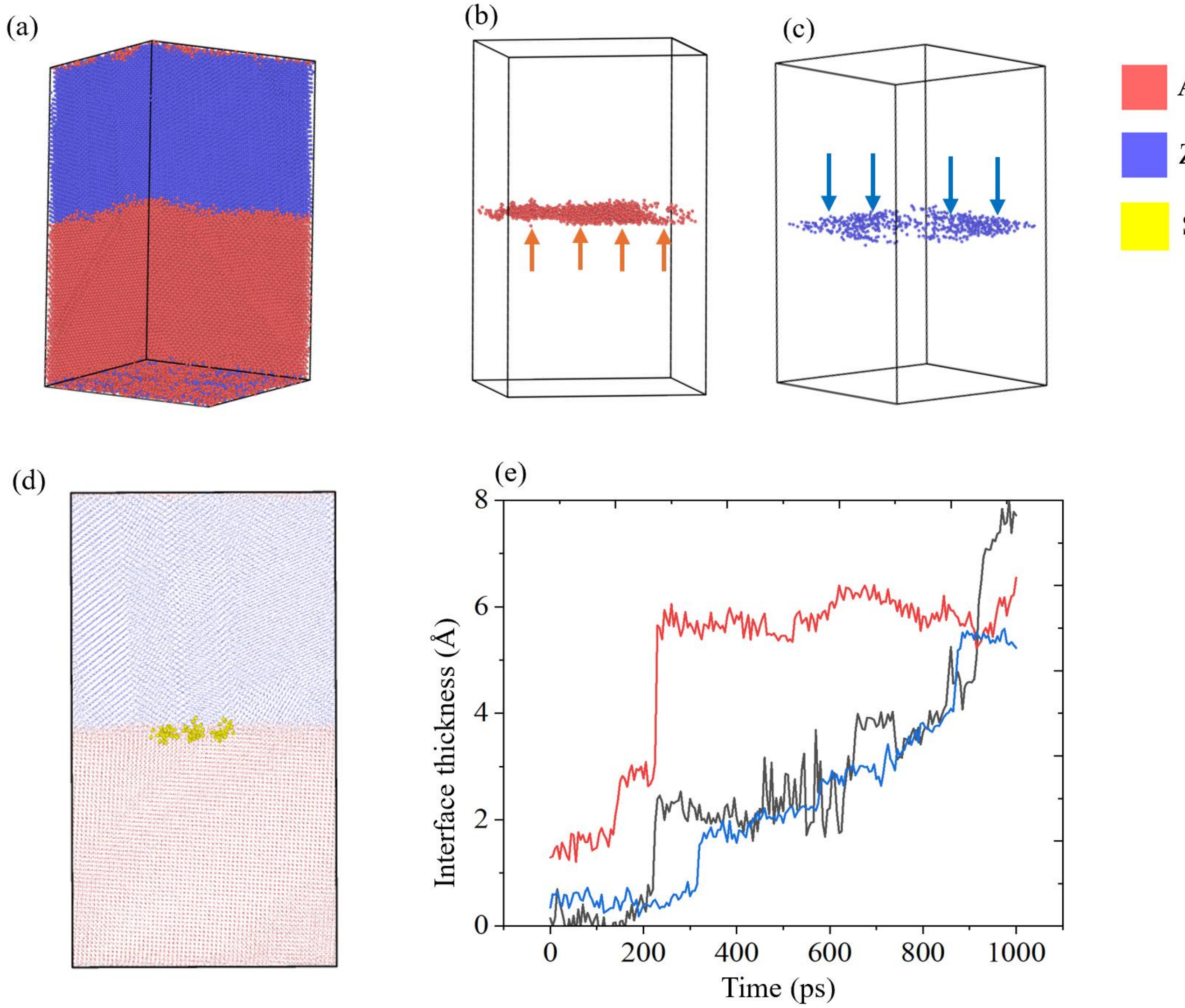

Figure 6: The Al-Zr system after undergoing HIP, illustrating atomistic deformation and migration across the interface 1 ns post-HIP initiation (a). Visualization exclusively of migrating aluminum atoms (b) and zirconium atoms (c), indicating their movements across the interface after 1 ns of HIP processing. (d) The spatial arrangement of silicon atoms, which preferentially migrate into the Al matrix following HIP. (e) Plot depicting the interfacial thickness at various HIP temperatures, all starting from identical initial configurations and subjected to consistent strain rates, black denotes 823 K, red denotes 770 K and blue denotes 723 K.

Interestingly, Figure 6 (d) shows Si atoms preferentially embedding themselves within the Al matrix rather than the Zr matrix post-HIP, aligning with experimental observations. This preference is supported by the formation of the Al_2SiZr intermetallic, attributed to Al’s smaller atomic radius (1.43 Å) compared to Zr (1.60 Å) and Al's lower melting point, which enhances its diffusivity at a given temperature. Figure 6 (e) reveals an increase in interface thickness over time, with a notable increase observed at higher temperatures (823 K, represented by the black line) due to the higher kinetic energy facilitating expedited diffusion.

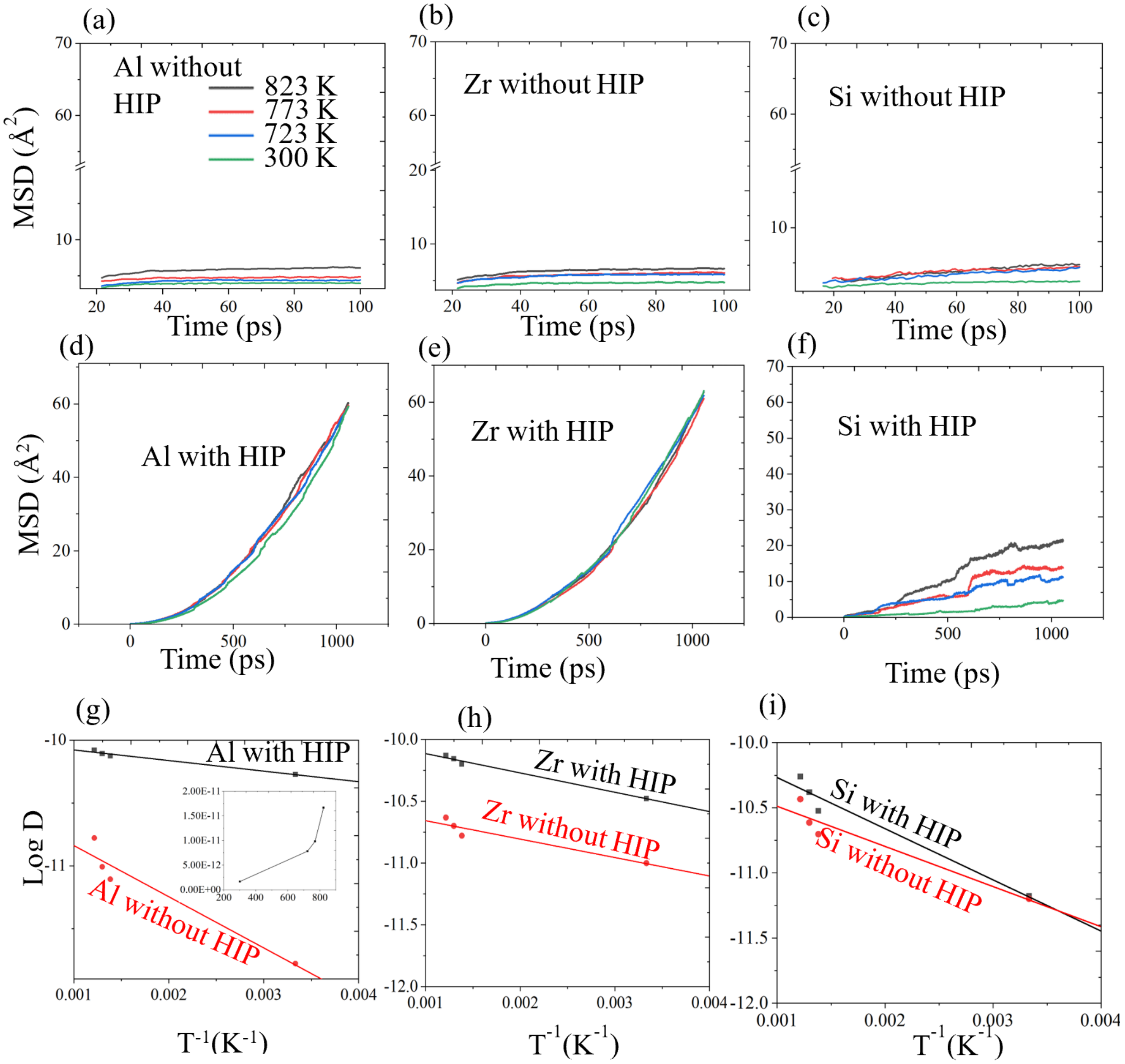

Figure 7: MSD analysis of constituent elements at temperatures of 300 K, 723 K, 773 K, and 823 K, comparing scenarios without HIP (a, b and c) and under HIP conditions for Al (d) Zr

(e) and Si (f). Subfigures (g), (h) and (i) present the Arrhenius plots, displaying the logarithm of the diffusion coefficient against the inverse absolute temperature for Al, Zr and Si respectively. The inset in (g) shows the diffusion coefficient of Al under non-HIP conditions, highlighting a clear knee at 723 K (450 °C), where an abrupt increase in diffusion occurs, consistent with the onset of interfacial transformations. The enhanced diffusion rates under HIP conditions are distinctly observed, with Al exhibiting a tenfold increase and Zr showing a 4-5 times increase in diffusion.

The resulting diffusion coefficients were calculated from the MSD curves generated by using the $D = \frac{1}{6}\partial\left(\frac{1}{N}\sum_{i=1}^{N}\langle\left(x_i(t) - x_i(0)\right)^2\rangle\right) / \partial t$ relation [23, 24]. Here, N is the total number of atoms in the molten state, and $x_i(t)$ is the position of i^{th} atom at time t. The obtained MSD curves for the combined system without the application of HIP are presented in Figure 7 (a-c) and with the application of HIP in Figure 7 (d-f) for Al, Zr and Si. In scenarios without HIP, the MSD curves stagnate soon, thus they were only simulated for 100 ps. But during HIP simulations, the timeframe is extended to 1 ns to allow sufficient time for the Al_2SiZr stoichiometry to be reached. MSD curves under HIP conditions show a steeper slope compared to those observed without HIP, attributed to the intensive plastic deformation experienced by the system. Such deformation-induced enhancements in diffusion rates for metal alloys are corroborated extensively in the literature [7, 26, 27]. An example study involving Ti diffusion in $Zr_{44}Ti_{11}Cu_{9.8}Ni_{10.2}Be_{25}$ demonstrated the increment of diffusion rates under plastic deformation in [26]. In metallic alloys, deformation-induced dislocations [28-31] can act as "fast diffusion pipes," enhancing atomic diffusivity [32]. Similar phenomenon is observed in the diffusion bonding process of Cu-Ag, where interfacial thickness increases under applied compressive stress [33]. These studies affirm the role of plastic deformation in adding diffusion pathways that becomes important in materials processing and interfacial engineering.

Table 3: A tabulation of diffusion data for Al, Zr and Si with and without HIP.

Host phase	D_0 (m^2/s)	Q_d (kJ/mol)
Al (no HIP)	4.88×10^{-9}	37.30
Zr (no HIP)	3.18×10^{-10}	16.60
Si (no HIP)	6.08×10^{-9}	29.91

Al (HIP)	1.86×10^{-10}	5.20
Zr (HIP)	2.56×10^{-10}	7.8
Si (HIP)	3.95×10^{-9}	30.61

Figure 7 (g-i) provides the logarithm of the diffusion coefficient plotted against the reciprocal absolute temperature for Al, Zr and Si under both HIP conditions and without HIP. Al demonstrates a substantial increase in diffusion rates under HIP, wherein the diffusion coefficient rises by nearly an order of magnitude, transitioning from 10^{-11} m^2/s to 10^{-10} m^2/s. This pronounced increase can be explained by lower melting point of Al, which makes it more prone to the synergistic effects of pressure and temperature applied during HIP. Zr experiences smaller increase in diffusion, characterized by a factor of 4-5 increase from $10^{-10.5}$ to 10^{-10} m^2/s. This behavior is attributable to the higher melting point of Zr, which provides greater lattice stability under HIP conditions, thereby lowering the extent of atomic migration. The inset in Figure 7 (g) illustrates the temperature dependence of Al diffusion under non-HIP conditions with distinct inflection point at 723 K (450 °C). This knee signifies a sharp increase in diffusivity, which aligns with the temperature at which interfacial phase formation initiates in the absence of HIP [2].

The tabulated diffusion data in Table 3 includes D_0, the temperature-independent pre-exponential factor, and Q_d, the activation energy for diffusion. Under HIP, both Al and Zr exhibit lower Q_d values, indicative of less energy required to initiate diffusion, a consequence of the structural perturbations and enhanced atomic mobility facilitated by the applied pressure and temperature. D_0, derived from the slope of the Arrhenius plot (Log D vs. 1/T), does not directly represent diffusion rates, but implies a decrease in the diffusion coefficient's dependence on temperature, which is reflected as a lower slope on the Arrhenius plot (log D vs. 1/T). This phenomenon indicates that, under HIP conditions, the enhancement of diffusion is less reliant on thermal activation as compared to ordinary conditions.

Si shows negligible variation in diffusion characteristics between HIP and non-HIP conditions, as depicted in Figure 7 (i). This stability is largely attributed to Si's initial placement at the interface, where it executes localized diffusion jumps to integrate into the Al_2SiZr phase. The interfacial role of Si focuses on structural alignment rather than extensive migration, which corresponds with the limited impact of temperature and pressure shifts during HIP. Its invariant behavior suggests a crucial stabilizing role within the Al-Zr matrix, primarily as a trigger for intermetallic formation rather than as a migrating species.

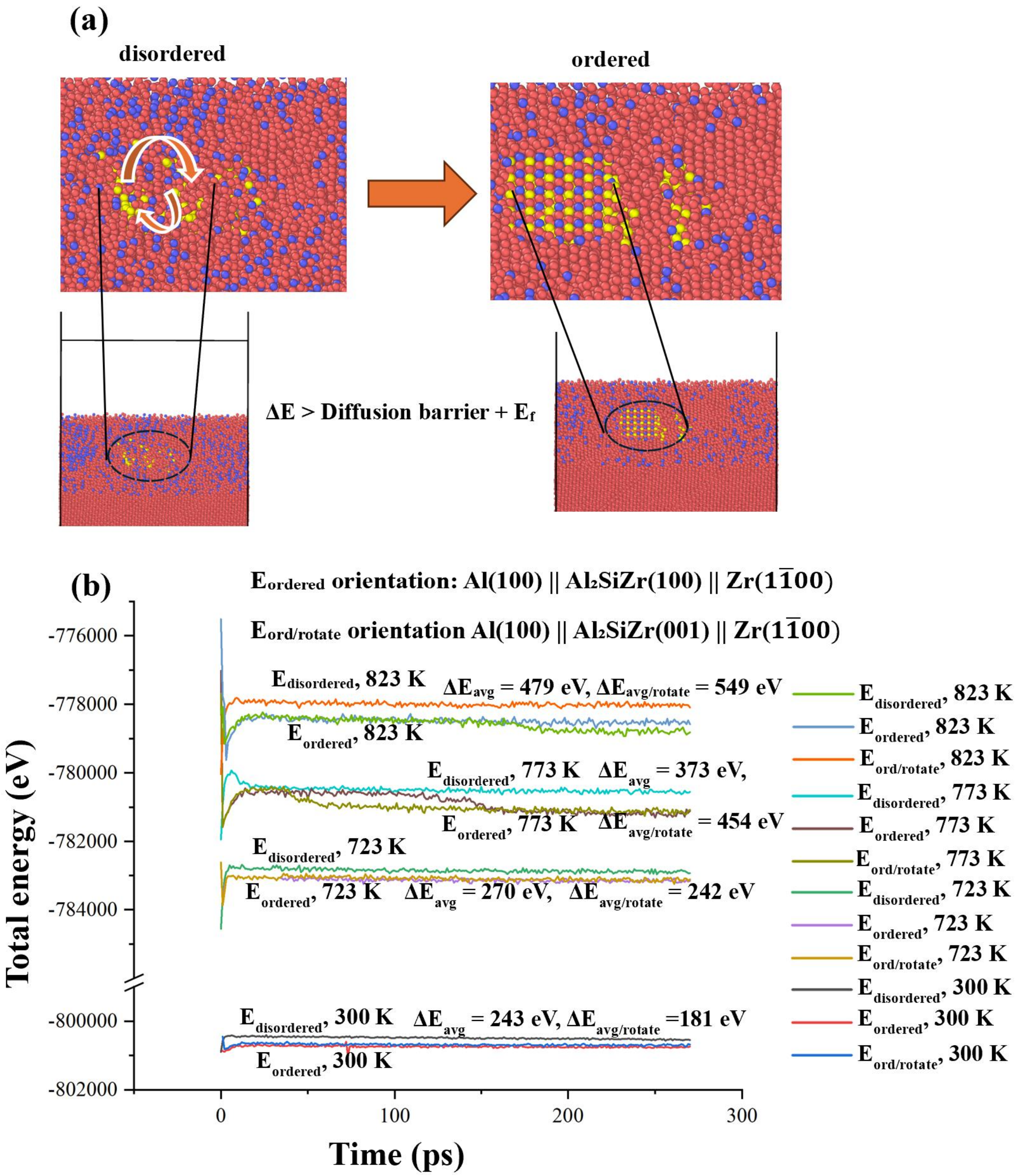

Figure 8: (a) Schematic representation of the microstructural evolution from a disordered to an ordered Al_2SiZr phase, showing the atomic diffusion jumps necessary for the formation of the ordered Al_2SiZr intermetallic structure. The total energy required for this

transformation includes both the formation energy of the Al_2SiZr phase and the energy associated with atomic migration. (b) A quantitative analysis of energy changes, illustrating the impact when the disordered region with Al_2SiZr stoichiometry transitions to an ordered structure. The orientation for the configuration depicted as $E_{ordered}$ is Al(100) || Al_2SiZr(100) || Zr($1\bar{1}00$) while that for $E_{ord/rotate}$ is Al(100) || Al_2SiZr(001) || Zr($1\bar{1}00$).

To elucidate the fundamental mechanism driving the formation of the secondary Al_2SiZr phase at the interface, we investigate the thermodynamic and kinetic requirements for this transformation. As outlined in the Methods section, we model the phase transition by substituting the interfacial zone with an ordered Al_2SiZr phase (Figure 8 (a)), thereby simulating the final configuration of a possible transformation pathway. Figure 8 (b) shows a quantitative analysis of energy changes when the disordered region with Al_2SiZr stoichiometry transitions to an ordered structure. ΔE_{avg} represents the drop in energy when the disordered structure changes to ordered Al2SiZr. When Al(100) || Al_2SiZr(100) || Zr($1\bar{1}00$) orientation is used at 773 K, the ΔE_{avg} is 373 eV and when a rotated orientation $E_{ord/rotate}$ Al(100) || Al_2SiZr(001) || Zr($1\bar{1}00$) is used the ΔE_{avg} increase to 454 eV. At a higher temperature of 823 K ΔE_{avg} values for both orientations increase and a lower temperatures ΔE_{avg} values for both orientations decrease as shown in Figure 8 (b). These results confirm that the energy reduction associated with ordering occurs consistently, regardless of the orientation of the inserted Al_2SiZr phase.

We hypothesize that the phase transition requires both (1) atomic rearrangement to conform to the ordered Al_2SiZr lattice and (2) sufficient energy input to overcome the charge transfer and bonding reconfiguration associated with compound formation. Therefore, the total energy required to complete this transformation includes both the formation energy of Al_2SiZr and the diffusion barriers associated with Al, Si, and Zr atom migration.

The formation energy per atom of Al_2SiZr is calculated using DFT-based data from the Materials Project. The total compound energy is expressed as:

$$\sum_i n_i \; E_f + \sum_i n_i \; E_i = E_{compound}$$

Using E_{Al_2SiZr}=-23.28 eV , $E_{Al} = -3.74\, eV/atom$, $E_{Si} = -5.42\, eV/atom$ and $E_{Zr} = -8.5\; eV/atom$ and n = 4, we get

$$E_f = \frac{E_{compound} - \sum_i n_i \; E_i}{n_{total}}$$

For a simulation cell with 408 atoms (204 Al, 102 Si, and 102 Zr), the total formation energy is:

$$E_f^{total} = 408 \times (-0.47 \; eV) = -191.76 \; eV$$

From diffusion calculations, we have Q_d Al = 0.05 eV/atom, Q_d Zr = 0.08 eV/atom and Q_d Si = 0.31 eV/atom. Importantly, these Q_d were extracted from non-HIP conditions, as the formation of the Al_2SiZr phase is observed to occur after the hot isostatic pressing (HIP) process has concluded. Post-HIP thermal exposure allows for continued atomic diffusion, albeit at reduced driving pressures, and governs the mobility required for the ordered phase to nucleate and grow. The total diffusion energy is calculated as:

$$Q_d^{total} = 204 \times 0.05 + 102 \times 0.31 + 102 \times 0.08 = 127.24 \; eV$$

Therefore, the total energy required for the formation of the Al_2SiZr phase is the sum of formation and diffusion energies:

$$E_{required} = \left| E_f^{total} \right| + Q_d^{total} = 191.76 + 127.24 = 319 \; eV$$

We then compare this required energy with the energy difference observed in our simulations after the interfacial transformation (Figure 8 (b)). At lower temperatures (300 K and 723 K), the available driving energies (~270 eV and ~243 eV, respectively) fall short of the estimated 319 eV required for full phase transformation, indicating that the process is energetically unfavorable at these temperatures. However, at higher temperatures, the system energy exceeds the required threshold, thereby enabling the atomic mobility and thermodynamic driving force necessary for Al_2SiZr phase formation. These results suggest that the onset of the phase transition is temperature-activated, driven by the combined effect of thermodynamic stability (negative formation energy) and sufficient atomic diffusion facilitated at elevated temperatures.

Conclusion

This study present the coupled thermodynamic and kinetic mechanisms governing Al_2SiZr phase formation in the Al-Si-Zr system under HIP conditions. Through MD simulations and diffusion analyses, we demonstrate that HIP enhances atomic mobility, enabling diffusion-driven phase transitions. Our results reveal that the formation of the Al_2SiZr intermetallic phase is contingent upon surpassing a critical energy threshold comprising both formation and diffusion energy barriers which occurs only at elevated temperatures. By integrating atomistic modeling with theoretical energy calculations, we provide a predictive framework for assessing phase transformation kinetics in alloy systems. The findings deepen understanding of the Al-Si-Zr interface behavior and reveal HIP's potential as a powerful process to engineer tailored microstructures in structural and nuclear materials.

Acknowledgements

This work was conducted at Pacific Northwest National Laboratory, which is operated by Battelle for the United States Department of Energy under contract DE-AC05-76RL01830. This work was funded by the U.S. Department of Energy National Nuclear Security Administration's Office of Material Management and Minimization.

References

[1] J. Dickson, L. Zhou, A.P. y Puente, M. Fu, D. Keiser Jr, Y. Sohn, Interdiffusion and reaction between Zr and Al alloys from 425 to 625 C, Intermetallics 49 (2014) 154-162.
[2] A. Mehta, J. Dickson, R. Newell, D.D. Keiser, Y. Sohn, Interdiffusion and reaction between Al and Zr in the temperature range of 425 to 475 C, Journal of Phase Equilibria and Diffusion 40 (2019) 482-494.
[3] A. Laik, K. Bhanumurthy, G. Kale, Single-phase diffusion study in β-Zr (Al), Journal of nuclear materials 305(2-3) (2002) 124-133.
[4] S. Hayes, J. Kennedy, B. Hilton, R. Fielding, T. Hyde, D. Keiser Jr, D. Porter, Metallic fuels, Nuclear Fuels & Materials Spotlight (Ed., KO Pasamehmetoglu), Idaho National Laboratory (2009) 21-41.
[5] M. Song, R. Kalsar, C. Miller, N. Overman, K.I. Johnson, T. Roosendaal, C. Lavender, V.V. Joshi, Correlation between Interface Microstructure and Bond Strength of Al6061/Al6061 HIP-Bonded Plates for Fuel Cladding Application, Materialia 23 (2022) 101458.
[6] R. Kalsar, N. Overman, T. Mason, M. Song, T. Roosendaal, K. Johnson, C. Miller, C. Lavender, V.V. Joshi, Insight into the interfacial microstructure and chemistry of hot isostatically pressed AA6061-AA6061 bonds for U-10Mo fuel cladding application, Journal of Nuclear Materials 599 (2024) 155193.
[7] A. Roy, R. Kalsar, M. Song, V.V. Joshi, Atomistic simulations to reveal HIP-bonding mechanisms of Al6061/Al6061, Acta Materialia 281 (2024) 120402.
[8] J.L. Snelgrove, G. Hofman, M. Meyer, C. Trybus, T. Wiencek, Development of very-high-density low-enriched-uranium fuels, Nuclear engineering and design 178(1) (1997) 119-126.
[9] J. Gan, B. Miller, D. Keiser Jr, A. Robinson, J. Madden, P. Medvedev, D. Wachs, Recent Development in TEM Characterization of Irradiated RERTR Fuels, Idaho National Lab.(INL), Idaho Falls, ID (United States), 2011.
[10] D. Keiser Jr, A. Robinson, M. Finlay, Observations derived from the characterization of monolithic fuel plates irradiated as part of the RERTR6 experiment, Argonne National Laboratory, Nuclear Engineering Division, RERTR Department ..., 2008.

[11] A. Robinson, G. Chang, D. Keiser Jr, D. Wachs, D. Porter, Irradiation performance of u-mo alloy based ‘monolithic’plate-type fuel–design selection, Idaho National Lab.(INL), Idaho Falls, ID (United States), 2009.

[12] D. Keiser, J. Jue, A. Robinson, P. Medvedev, M. Finlay, SEM Characterization of an Irradiated Dispersion Fuel Plate with U-10Mo Particles and 6061 Al Matrix, Idaho National Lab.(INL), Idaho Falls, ID (United States), 2009.

[13] G. Moore, J. Jue, B. Rabin, M. Nilles, Full size U-10Mo monolithic fuel foil and fuel plate fabrication-technology development, Idaho National Lab.(INL), Idaho Falls, ID (United States), 2010.

[14] K. Huang, Y. Park, D. Keiser Jr, Y. Sohn, Interdiffusion between Zr diffusion barrier and U-Mo alloy, Journal of Phase Equilibria and Diffusion 33(6) (2012) 443-449.

[15] J. Crapps, K. Clarke, J. Katz, D.J. Alexander, B. Aikin, V.D. Vargas, J.D. Montalvo, D.E. Dombrowski, B. Mihaila, Development of the hot isostatic press manufacturing process for monolithic nuclear fuel, Nuclear engineering and design 254 (2013) 43-52.

[16] K.D. Clarke, C.E. Cross, R.E. Hackenberg, R.J. McCabe, J.D. Montalvo, M.J. Dvornak, R.L. Edwards, J.M. Crapps, R.R. Trujillo, B. Aikin, Development of aluminum-clad fuel plate processing through canned and canless hot isostatic pressing (HIP), and studies of aluminum cladding grain growth during HIP, Reduced Enrichment for Research and Test Reactors (RERTR) (2012).

[17] S. Plimpton, Fast parallel algorithms for short-range molecular dynamics, Journal of computational physics 117(1) (1995) 1-19.

[18] G. Plummer, G.J. Tucker, Bond-order potentials for the Ti 3 AlC 2 and Ti 3 SiC 2 MAX phases, Physical Review B 100(21) (2019) 214114.

[19] M.S. Daw, J.W. Lawson, C.W. Bauschlicher Jr, Interatomic potentials for zirconium diboride and hafnium diboride, Computational materials science 50(10) (2011) 2828-2835.

[20] J. Tersoff, Modeling solid-state chemistry: Interatomic potentials for multicomponent systems, Physical review B 39(8) (1989) 5566.

[21] J. Kristensen, N.J. Zabaras, Predicting low-thermal-conductivity Si-Ge nanowires with a modified cluster expansion method, Physical Review B 91(5) (2015) 054105.

[22] A. Jain, S.P. Ong, G. Hautier, W. Chen, W.D. Richards, S. Dacek, S. Cholia, D. Gunter, D. Skinner, G. Ceder, Commentary: The Materials Project: A materials genome approach to accelerating materials innovation, APL materials 1(1) (2013) 011002.

[23] D. Frenkel, B. Smit, Understanding molecular simulation: from algorithms to applications, Elsevier2023.

[24] A. Roy, J. Munshi, G. Balasubramanian, Low energy atomic traps sluggardize the diffusion in compositionally complex refractory alloys, Intermetallics 131 (2021) 107106.

[25] G. Wu, K. Dash, M. Galano, K. O’Reilly, Oxidation studies of Al alloys: part II Al-Mg alloy, Corrosion Science 155 (2019) 97-108.

[26] A. Lee, S.Y. Kim, H. Jang, Y. Kim, F. Spieckermann, G. Wilde, J. Eckert, M. Lee, Strain perceptibility of elements on the diffusion in Zr-based amorphous alloys, Scientific Reports 10(1) (2020) 4575.

[27] C. Salsi, D. Monceau, C. Desgranges, T. Gheno, Effect of Compressive Creep and Hydrostatic Pressure on Diffusion in NiCr and NiSi Systems, Metallurgical and Materials Transactions A 53(12) (2022) 4247-4257.

[28] G. Love, Dislocation pipe diffusion, Acta Metallurgica 12(6) (1964) 731-737.

[29] A. Sharma, G. Balasubramanian, Dislocation dynamics in Al0. 1CoCrFeNi high-entropy alloy under tensile loading, Intermetallics 91 (2017) 31-34.

[30] A. Roy, R. Devanathan, D.D. Johnson, G. Balasubramanian, Grain-size effects on the deformation in nanocrystalline multi-principal element alloy, Materials Chemistry and Physics 277 (2022) 125546.

[31] A. Roy, C. Burns, S. Livers, B. Lund, S. Meher, M.S.K.K.Y. Nartu, A. Mahmud, T. Wang, D. Garcia, J. Dos Santos, Critical mineral substitutions in IN617: A combined computational and experimental approach to performance evaluation and feasibility, Materialia 39 (2025) 102319.
[32] J. Robson, Deformation enhanced diffusion in aluminium alloys, Metallurgical and Materials Transactions A 51(10) (2020) 5401-5413.
[33] S. Chen, A. Soh, F. Ke, Molecular dynamics modeling of diffusion bonding, Scripta Materialia 52(11) (2005) 1135-1140.